






Article

Detailing the Self-Discharge of a Cathode Based on a Prussian Blue Analogue

Elisa Musella ¹, Angelo Mullaliu ¹, Thomas Ruf ², Paula Huth ², Domenica Tonelli ¹,
Giuliana Aquilanti ³, Reinhard Denecke ^{2,*} and Marco Giorgetti ^{1,*}

¹ Department of Industrial Chemistry “Toso Montanari”, University of Bologna, Viale Risorgimento 4, 40136 Bologna, Italy; elisa.musella3@unibo.it (E.M.); angelo.mullaliu2@unibo.it (A.M.); domenica.tonelli@unibo.it (D.T.)

² Wilhelm-Ostwald-Institut für Physikalische und Theoretische Chemie, Universität Leipzig, Linnéstraße 2, D-04103 Leipzig, Germany; thomas.ruf@uni-leipzig.de (T.R.); paula.huth@uni-leipzig.de (P.H.)

³ Elettra Sincrotrone Trieste S.C.p.A., s.s. 14 km 163.5, 34149 Basovizza, (TS), Italy; giuliana.aquilanti@elettra.eu

* Correspondence: denecke@uni-leipzig.de (R.D.); marco.giorgetti@unibo.it (M.G.); Tel.: +49-341-97-36500 (R.D.); +39-051-209-3666 (M.G.); Fax: +49-341-97-36399 (R.D.)

Received: 11 July 2020; Accepted: 31 July 2020; Published: 4 August 2020



Abstract: Prussian Blue analogues (PBAs) are a promising class of electrode active materials for batteries. Among them, copper nitroprusside, $\text{Cu}[\text{Fe}(\text{CN})_5\text{NO}]$, has recently been investigated for its peculiar redox system, which also involves the nitrosyl ligand as a non-innocent ligand, in addition to the electroactivity of the metal sites, Cu and Fe. This paper studies the dynamics of the electrode, employing surface sensitive X-ray Photoelectron spectroscopy (XPS) and bulk sensitive X-ray absorption spectroscopy (XAS) techniques. XPS provided chemical information on the layers formed on electrode surfaces following the self-discharge process of the cathode material in the presence of the electrolyte. These layers consist mainly of electrolyte degradation products, such as LiF , $\text{Li}_x\text{PO}_y\text{F}_z$ and Li_xPF_y . Moreover, as evidenced by XAS and XPS, reduction at both metal sites takes place in the bulk and in the surface of the material, clearly evidencing that a self-discharge process is occurring. We observed faster processes and higher amounts of reduced species and decomposition products in the case of samples with a higher amount of coordination water.

Keywords: copper nitroprusside; XPS; XAS; self-discharge; electrolyte degradation

1. Introduction

In the last century, global energy demand has grown remarkably, and all the indicators suggest it will keep on increasing in the next few decades [1]. Therefore, one of the focuses for further development is to find new solutions in terms of energy storage devices [2]. To date, the lithium ion technology is the most mature technology [3,4]. In fact, Li-ion batteries are key components in portable devices and the computing and telecommunication tools required daily by society [5].

The principal challenges that these devices have faced in real-life application are cost, safety and service life. In particular, the points that need to be considered to lower costs are automation of manufacturing, material density, rate capabilities and service life. To guarantee long service life, avoiding undesired chemical reactions between the electrolyte and the electrodes could be one of the keys [2].

Among these challenges, the comprehension of complex surface reactions at the electrode–electrolyte interface is a longstanding problem in Li-ion batteries, since surface chemistry has been proven to be limiting for battery development [6–9].

In general, active materials are characterized by a complex chemical surface behavior. However, full understanding and optimization of the commonly employed carbonate-based electrolyte solutions

have not been achieved yet. In fact, the precise structure, composition and functional mechanism(s) remain under debate [10]. In any case, it is quite well established that surface stability is one of the fundamental contributions to obtain enhanced battery performance [11]. The choice of the electrolyte directly influences the battery lifetime; therefore, electrolyte solutions need to be unalterable at operating potentials and to form stable electrode/electrolyte interphases [12].

The phenomenon of self-discharge occurs when a battery, which is at full or partial state of charge (SOC), experiences the loss of its capacity under open circuit conditions due to chemical reactions within the cell. The kinetics depends on the battery chemistry, electrode and electrolyte formulation and impurities and on the storage temperature [13]. It is possible that the lost capacity is partially restored after a recharge.

Several factors are involved in battery self-discharge. In particular, electron leakage is one of the main contributions. This may be due either to internal shorts, or to the partial electronic conductivity of the electrolyte, or to the poor insulating properties of the battery seals. Moreover, the electrode/electrolyte reactions (e.g., anode corrosion and cathode reduction), the partial dissolution of the active material and the passivation deriving from decomposition products can contribute at different extents to capacity loss [13].

Among the different listed processes involved in the battery self-discharge, phenomena related to the reduction of non-aqueous solutions, leading to the creation of a passive layer based on the inorganic and organic electrolyte decomposition products, are some of the most interesting.

The most studied passivation layer—i.e., the solid electrolyte interphase (SEI)—tends to form at anodic electrodes [14–19]. In the ideal case, it prevents the electron transport, avoiding further electrolyte degradation, and concomitantly it allows the transport of Li-ions upon cycling. Surface phenomena on positive electrodes are studied much less frequently with respect to negative electrodes. This does not mean they are of less importance; in fact, they have been drawing a lot of attention lately [7,12,18,20]. Even though interface phenomena also happen at the cathodic side, the validity of the SEI-layer concept is still tenuous in this context. In this case, Li⁺ ions must also pass through an additional layer, called cSEI—i.e., cathode solid electrolyte interphase—which lies between the cathode and the electrolyte solution and which has even been proven to be rate-limiting [6]. The term “cSEI” is commonly used to refer to a film formed at the cathodic side, with the SEI and cSEI being significantly different in terms of both composition and properties [20].

As already reported in the literature [14], an investigation of the cSEI has been carried out through a multi-technique approach, involving X-ray photoelectron spectroscopy (XPS) [10,14,21,22], Fourier-transform infrared spectroscopy (FTIR) [23,24], and NMR spectroscopy [17,25]. Li et al. studied the self-discharge of a layered lithium rich oxide cathode when an additive is added to the electrolyte [26].

Moreover, the development of new active materials for cathodes has been the main focus—among all possibilities, Prussian Blue analogues (PBAs) are a promising class of materials [27]. PBAs are bimetallic cyanides with a 3D lattice of repeating -Fe-CN-M-NC- units, with M being a transition metal, such as Zn, Cu, Ni, Co and Mn. Copper nitroprusside, Cu[Fe(CN)₅NO] (CuNP), has been recently investigated for its peculiar redox system, which also involves the nitrosyl ligand as a non-innocent ligand [28,29].

In this work, we report a study aimed at the understanding of the self-discharge process occurring at two copper nitroprusside electrodes (which differ in the amount of hydration water) employing a surface sensitive technique—XPS—and a bulk sensitive one—X-ray absorption spectroscopy (XAS)—in order to gain complementary information.

2. Materials and Methods

2.1. Material Synthesis and Electrode Preparation

The synthesis of the active material (copper nitroprusside) was based on a co-precipitation method from an aqueous solution containing 20 mM CuSO₄·5H₂O (Code 209198) and Na₂[Fe(CN)₅(NO)]·2H₂O

(Code 71778), used as purchased from Sigma-Aldrich, and discussed in a previous work [29]. The material was formulated into pellets with the following composition: 70% *w/w* active material, 10% *w/w* PTFE (Teflon), 10% *w/w* CB (Carbon Black) and 10% *w/w* VGCF_H (Vapor Grown Carbon Fiber). Disks were cut from the flattened paste using a puncher with an inner diameter of 8 mm. The mass loading of such disks was 6–8 mg cm⁻² of active material and 1 M LiPF₆ in an ethylene carbonate (EC), propylene carbonate (PC) and dimethyl carbonate (DMC) volumetric mixture (EC:PC:DMC = 1:1:3) without additives was used as an electrolyte. Two different copper nitroprusside powders were obtained with different amounts of hydration water in the structure: Cu_{0.8}Fe_{1.2}(CN)₅(NO)·0.2H₂O (sample I), and CuFe(CN)₅(NO)·2.2H₂O (sample II). The stoichiometry was calculated by means of atomic absorption spectroscopy and X-ray Fluorescence Spectroscopy. The amount of water was derived from thermogravimetric analysis (TGA). Unlike as the precursor salts would indicate, the oxidation states of the iron in pristine copper nitroprusside is not consistent with the simple presence of Fe(II), as verified previously by XANES and by ⁵⁷Fe Mössbauer studies [29]. The electrodes analyzed have never been submitted to any electrochemical procedure; however, we still refer to the reduction processes as “self-discharge”.

2.2. Material Characterization

XPS measurements and data analysis: XPS measurements were recorded by a VG Escalab 220i-XL spectrometer equipped with a model 220 analyzer and a set of six channel electron multipliers with a multidetector dead time of 16 ns. Al K_α (E = 1486.6 eV) radiation from an aluminum-magnesium twin anode source was used for all samples, along with pressures in the analysis chamber of 10⁻⁹–10⁻⁸ mbar. A pass energy of 50 eV was chosen for survey spectra, while 20 eV were used for detailed spectra. Measurements were made taking care that the exposure to UHV and to X-rays were the same for all samples in order to minimize modifying effects. The spectra were analyzed and fitted by UNIFIT 2020 [30]. A Shirley function was chosen for the fitting of the background. Line syntheses of detailed spectra were conducted using a Voigt profile [31]. The formulated electrode samples were washed with acetone before being fixed on a sample holder with carbon tape and inserted in the XPS machine. No treatment was carried out for the soaked electrodes. The soaked electrode samples were prepared as follows: (i) preparation of the coin cells; (ii) 6 months rest period; (iii) cell disassembly, extraction of the cathodes and XPS measurement.

For the assignment of the deconvoluted peaks, NIST XPS database or the “identify lines” tool of the UNIFIT 2020 was used as well as literature references [9]. The alignment of the binding energy scale was made through N 1 s signal of cyanide (397.2 eV) [32]. Normalized areas for quantification were derived using proper sensitivity factors.

XAS measurements and data analysis: XAS experiments were performed at Elettra Sincrotrone Trieste (Italy), at the XAFS beamline [33]. The storage ring operated at 2.0 GeV in top up mode with a typical current of 310 mA. XAS data were recorded at Fe and Cu K-edges in transmission mode on the pristine and aged electrode by using ionization chambers filled with a mixture of Ar, N₂ and He to have 10%, 70% and 95% of absorption in the I₀, I₁ and I₂ chambers. An internal reference of iron and copper foil was used for energy calibration. The energies were calibrated by assigning the first inflection point of the spectra of the metallic iron and copper to 7112 eV and 8979 eV, respectively. Spectra at the Fe and Cu K-edges were collected with a constant k-step of 0.03 Å⁻¹ with a 2 s/point acquisition time. Data were collected from 6900 to 8000 eV for Fe K-edge and from 8750 to 9830 eV for the Cu K-edges. The energy selection of the synchrotron beam was done by using a fixed exit monochromator equipped with a pair of Si(111) crystals. Harmonics rejection was done by using the cutoff of the reflectivity of the platinum mirror placed at 3 mrad with respect to the beam upstream (Cu K-edge) or by detuning the second crystal of the monochromator by 30% of the maximum (Fe K-edge).

3. Results and Discussion

3.1. Powder Characterization

Figure 1a displays the X-ray photoelectron response (survey spectrum) of sample I to summarize all the elements' signals present in the powder ranging from carbon to iron. In Figure 1b, it is possible to notice that the $-\text{CN}$ group and the adventitious carbon (as contaminants) are mainly contributing to the C 1s. From Figure 1c, N 1s can be described as the contribution of $-\text{NO}$ and $-\text{CN}$ groups, as expected from the compound formula. From Figure 1d, O 1s comprises three main species—i.e., $-\text{NO}$ group, water and the oxygen coming from adventitious species. The $-\text{NO}$ group and water (besides some adsorbed water) are expected to be present in the material, while we can address the third signal as an impurity—probably some carbonate species from the adsorption of CO_2 . From Figure 1e, it is possible to observe the contribution of two main peaks—i.e., Cu $2p_{3/2}$ and Cu $2p_{1/2}$ at 934 and 954 eV, respectively. The deconvoluted spectrum suggests the presence of two coexisting oxidation states: Cu^+ (932 eV) and Cu^{2+} (935.2 eV) plus the satellite (942 eV) [34,35]. Only Cu^{2+} was expected from the stoichiometry of the precursor salts and, in fact, it is the dominant species. From Figure 1f, the Fe 2p signal shows the typical feature of the $2p_{3/2}$ and $2p_{1/2}$ doublet (at 710 and 722 eV, respectively). Detailing the Fe $2p_{3/2}$ signal, it shows the contribution of two main species at 709.8 and 708.0 eV. Cano et al. [34] report that, although in the as-synthesized samples the metals (Cu, Fe) are expected in their divalent oxidation state, the recorded XPS spectra show peaks at lower binding energy with respect to the main peak, corresponding to the reduced species (Cu^+ , Fe^0). In our case, no component for Fe^0 was necessary to fit the signal and, therefore, detected in the sample (707.5 eV). These considerations led us to conclude that a partial sample degradation during the XPS experiment was happening. They also suggested the appearance of a high-spin Fe^{2+} species, in which the way the cyanide ligand bonds to the Fe atom was altered during the XPS measurement (from Fe-CN to Fe-NC). The Cu^+ species were, instead, identified as copper cyanide, CuCN, bringing further evidence to the breakage of the Fe-N-C bond. It is important to highlight that Cano et al. stated the observed decomposition effects have only a local character. They indeed assigned positions in the XPS spectrum as following: 710 eV for low-spin Fe(II), 708.8 eV for high-spin Fe(II) and 715 eV to a satellite [34]. Accordingly, we can also attribute our positions (709.8 and 708 eV) to a low-spin Fe(II) which has evolved locally to a high-spin one due to degradation under XPS measurement. Regarding copper, it is reported [36] that a certain amount of monovalent species is already present in the pristine material. Concerning the iron oxidation state, a previous XAS study available for sample I only suggests that the initial oxidation state of the Fe is better described as $\text{Fe}^{\text{II}+\delta}$ [37]. Sample II displays very similar peak profiles for the core levels under study (see Figure S1 for spectra of sample II). Table 1 summarizes all positions and attributions related to CuNP samples.

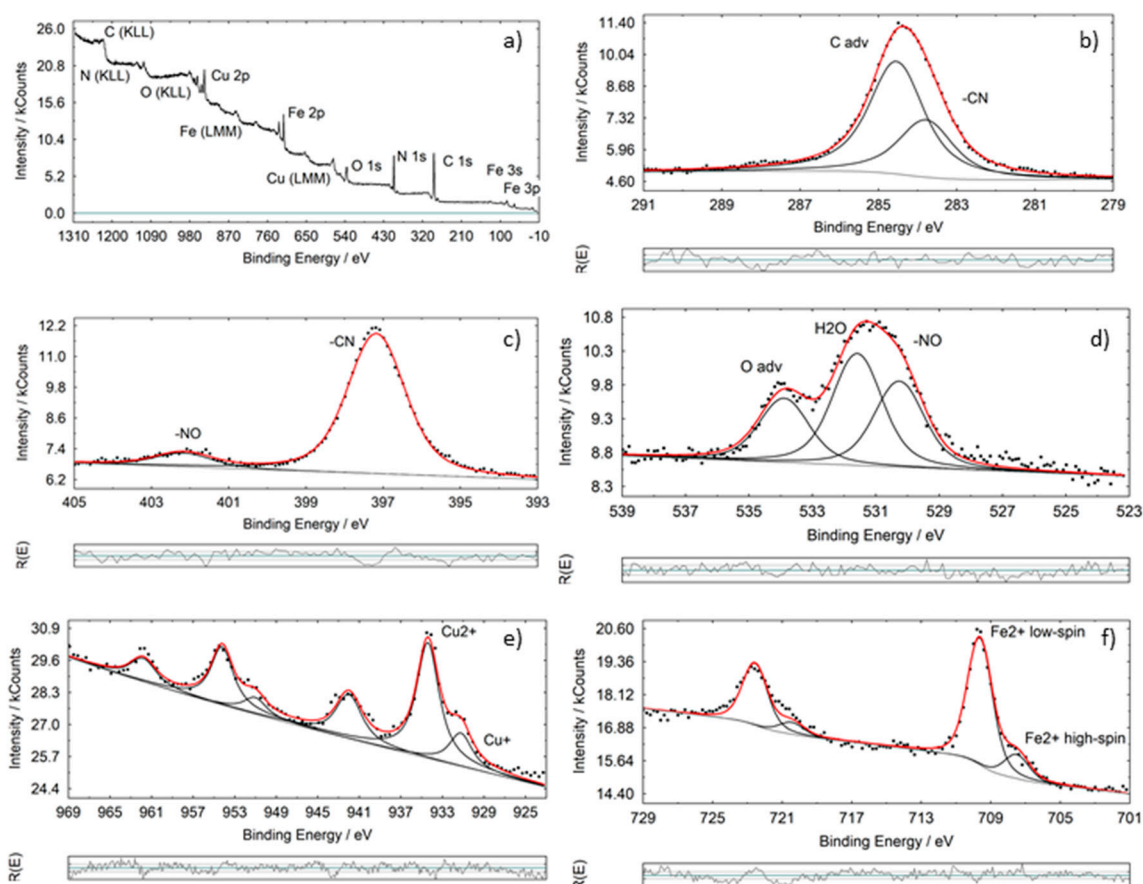


Figure 1. XPS fitted data of copper nitroprusside I. The detailed spectra reported are (a) survey (b) C 1s (c) N 1s (d) O 1s (e) Cu 2p and (f) Fe 2p (in red: sum of fitting result; solid lines: background or peak contribution).

Table 1. Values of binding energies (in eV) for CuNPs samples.

	Binding Energies (eV)											
	C 1s		N 1s		O 1s			Cu 2p			Fe 2p	
	CN	Cadv	CN	NO	NO	H ₂ O	Cu (+)	Cu (2+)	Cu Sat	Fe (II) High Spin	Fe (II) Low Spin	Fe Sat
CuNP I	283.7	284.6	397.2	402.2	530.3	531.6	932.0	935.4	942.0	708.0	709.8	-
CuNP II	283.6	284.9	397.2	402.2	529.7	531.5	932.1	935.4	942.1	708.2	710.2	-
Ref [33]	283.4/284.3	284.8	397.2/397.8	402.6	530.8	532.1	932.4	936	941.8	708.8	710.1	714.8

In Table 2 the quantification of the species is also reported for both samples.

Table 2. XPS quantification (normalized areas) of sample I and II. The value of N (NO) was set to 1.

	C 1s (CN)	N 1s (CN)	N 1s (NO)	O 1s (NO)	Cu 2p	Fe 2p	Formula	Expected Formula
I	6.1	6.4	1	1.1	0.9	1.0	Cu _{0.9} Fe ₁ (C _{6.1} N _{6.7})(N _{1.0} O _{1.1})	Cu _{0.8} Fe _{1.2} (CN) ₅ (NO)
II	6.5	6.7	1	1.0	1.7	1.4	Cu _{1.7} Fe _{1.4} (C _{6.5} N _{6.7})(NO) ₁	CuFe(CN) ₅ (NO)

In Table 2, the quantification of the species is also reported for both samples. It can be observed that, in general, the main parts of the formula—e.g., NO, CN and the ratio between Cu and Fe, reflect the expectations. Nevertheless, deviations such as the apparently higher CN content in both samples or the higher metal content in sample II could be traced back to surface contaminations [38] or uncertainties in the analysis procedure. However, for such reasons, XPS is used here mainly for elucidating the chemical states (i.e., oxidation states or bond motifs) of the elements involved.

XAS experiments were conducted on the powders in transmission mode. XAS is a bulk technique able to gain complementary information with respect to surface sensitive XPS. XAS spectra at Fe and Cu K-edges of the materials give information on the charge of the absorbing atom and its local coordination geometry. Figure 2 displays the X-ray absorption near the edge structure (XANES) signals at both Fe and Cu K-edges for both samples. The signals arising from samples I and II are superimposable, suggesting the same local coordination geometry and charge for these two materials. How much could that charge be? XANES traces feature a pre-edge signal due to a transition to bound states, which corresponds to the dipole-forbidden but quadrupole-allowed $1s-3d$ transition. The pre-edge energy position and the shape of this transition can be used as an indicator of the formal oxidation state of the photoabsorber metal. They are visible at around 7114 for the Fe K-edge and as a weak signal at 8978 eV for the Cu K-edge (two zooms of the spectra are available in Figures S2 and S3). Previous XANES data for sample I reported a formal oxidation state for the iron between (+2) and (+3); therefore, the state can be described as $Fe^{II+\delta}$ [37]. Here, that assignment is also valid for sample II. In addition, the overall shape of the XANES curves suggests an octahedral geometry around the metal in both pristine materials. For the Cu K-edge, the overall XANES spectra display Cu in an octahedral environment [37], while the presence of a weak pre-edge peak at about 8978 eV is an indicator of Cu^{II} in both samples. To gain a better understanding of the atomic local structure, an EXAFS analysis was performed and the obtained results (reported in the Table S1) indicate a very similar metallic local environment in both compounds.

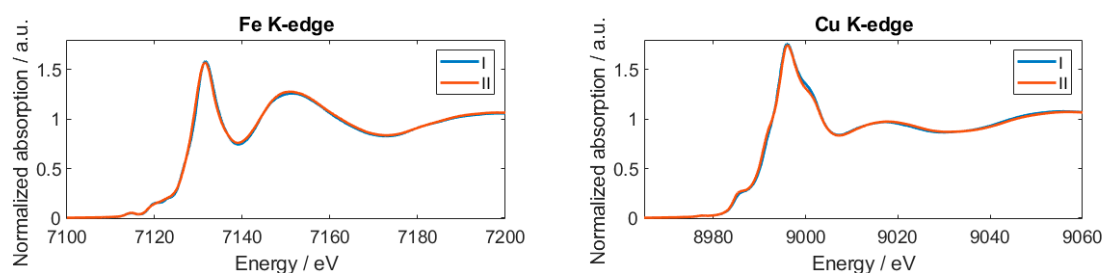


Figure 2. XANES traces at Fe and Cu K-edges for both samples I and II. Spectra were recorded on as-synthesized powders.

It might seem that small differences in the oxidation states of the two metals are detected with the two different techniques. It can be easily explained through the consideration that XPS is a surface sensitive technique, whereas XAS is a bulk sensitive one: it is indeed possible that the surface of the material can be affected by the exposure to air and vacuum, an effect that would be totally neglected when the bulk is investigated.

3.2. Formulated Pellet and Pellet in Contact with Electrolyte

To investigate the effect of the electrolyte on the pristine materials, formulated electrodes of samples I and II were soaked in the electrolyte for 6 months in order to make a comparison between powder and the as-prepared electrode. The study was conducted by considering both the surface (by XPS) and the bulk of the electrode (by XAS). This sets the relative importance of the electrolyte contact time in relation to the effects of the material state of charge that will be presented in the next section. Oxidation states of the two metals and the decomposition of the electrolyte will be taken into consideration.

The XPS spectra of the formulated electrodes left in contact with the electrolyte solution display a similar chemical composition with respect to the pristine formulated cathodes. Table 3 summarizes the quantification arising from the fitting of the XPS spectrum related to formulated electrodes and formulated electrodes soaked in the electrolyte to confirm the chemical identity with the above-mentioned powders. However, in the case of soaked samples, it was not possible to obtain a quantification for Fe 2p signals. In fact, as already reported for FeF_3 [39], the F 1s peak is very close in binding energy to the Fe $2p_{3/2}$ envelope and also quite intense, with some of its plasmon loss peaks

overlapping the peak of iron (Figure 3a). In general, it is possible to state that the electrolyte layer is strongly damping the signals of the electrode: all signals are quite weak due to the thick electrolyte layer, thus enhancing the error bars quite significantly. In light of that, all samples are considered highly similar.

Table 3. XPS quantification (normalized areas) of sample I and II formulated and soaked into the electrolyte. For soaked samples, the value of N (NO) was set to 1.

	C 1s (CN)	N 1s (CN)	N 1s (NO)	O 1s (NO)	Cu 2p	Fe 2p	Formula
I_formulated	6.1	6.8	1.0	1.1	1.1	1.3	$\text{Cu}_{1.1}\text{Fe}_{1.3}(\text{C}_{6.1}\text{N}_{6.8})(\text{N}_1\text{O}_{1.1})$
II_soaked	6.4	6.1	1.0	1.0	1.4	x	$\text{Cu}_{1.4}\text{Fe}_x(\text{C}_{6.4}\text{N}_{6.1})(\text{NO})_{1.0}$
II_formulated	6.7	6.8	1.0	1.0	1.5	1.7	$\text{Cu}_{1.5}\text{Fe}_{1.7}(\text{C}_{6.7}\text{N}_{6.8})(\text{NO})_{1.0}$
II_soaked	6.3	6.0	1.0	1.0	1.4	x	$\text{Cu}_{1.4}\text{Fe}_x(\text{C}_{6.3}\text{N}_{6.0})(\text{NO})_{1.0}$

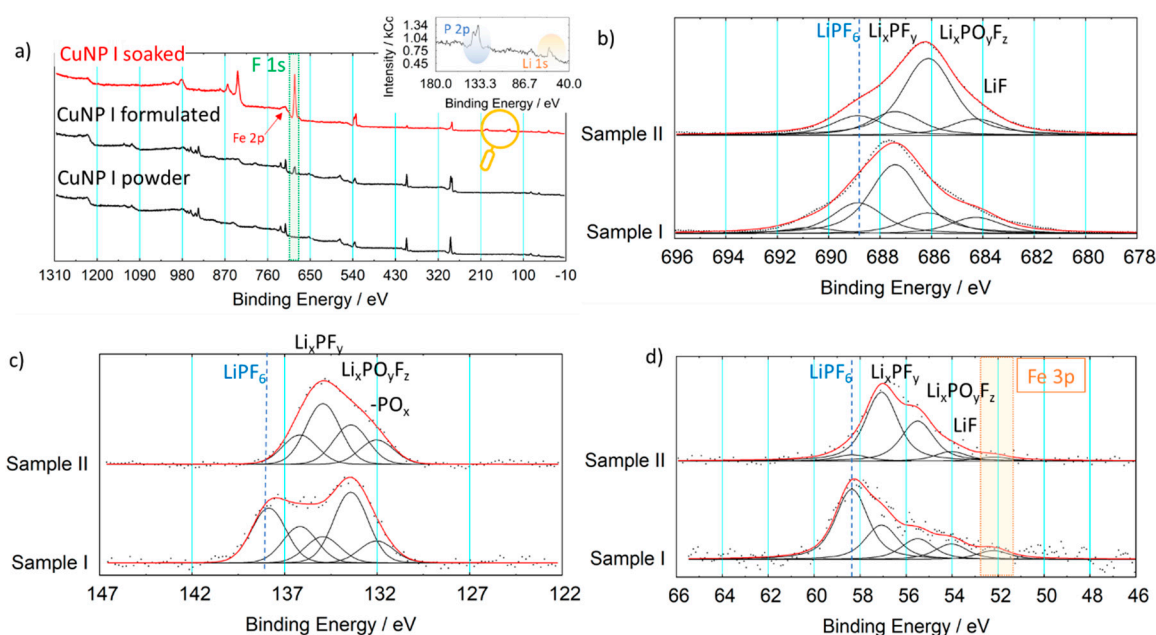


Figure 3. (a) Comparison of surveys of sample I. (b–d) Comparison between fitted data of the two samples. The detailed spectra reported are (b) F 1s (c) P 2p (d) Li 1s.

With the formulation of the electrodes, new XPS signals relevant to Teflon are expected to appear (in the F 1s spectrum). Moreover, by also adding the contribution of the electrolyte, the presence of Li 1s and P 2p in surveys can be detected. In Figure 3a, the comparison of survey spectra of sample I between powder, CuNP formulated and CuNP soaked is shown.

After the soaking of the electrode in the electrolyte, in the F 1s detailed spectrum, three new peaks associated with the formation of LiF, $\text{Li}_x\text{PO}_y\text{F}_z$, and LiPF_6 are also detected with respect to the formulated electrode, which displayed only Teflon-like species (Figure S4). In principle, the use of PTFE as a binder might hinder the proper evaluation of the peak: this is actually not the case. As it can easily be seen in Figure 3a, the intensity of F 1s is greatly enhanced when the electrolyte is encountered. In particular, the intensity of this signal for the formulated CuNP is around 2 kCounts, whilst the one for the sample that was soaked into the electrolyte is 11 kCounts. Furthermore, it can be assumed that the degraded Teflon products are buried under the electrolyte decomposition layer. Therefore, the photoelectron intensity of the “F 1s teflon components” is further attenuated. It can be approximated that around 63% of photoelectron intensity is derived from the first mean free path in XPS. So, the ratio for electrolyte components relative to the Teflon components will be more than 11/2.

Figure 3b–d display the comparison of F 1s signals, Li 1s and P 2p of sample I and sample II after being soaked in the electrolyte. With regard to the degradation of the electrolyte, the formation of

degradation products (cSEI: LiF, $\text{Li}_x\text{PO}_y\text{F}_z$ and Li_xPF_y) is indeed reported for a conventional LiCoO_2 cathode soaked in an electrolyte [21]. The presence of transition metals often favors decomposition processes at the electrolyte side by forming a thin layer of material on the electrode surface, even at rest condition—i.e., without current flowing. Specifically, for the LiPF_6 salt, the reactions 1–4 summarized below can be accelerated by the presence of traces of water inside the electrolyte [39], which in turn produces hydrofluoric acid (HF) and fluorophosphate-based species. Moreover, the PF_5 species produced in reaction 1 can further react with the hydroxyl groups, triggering the formation of POF-R-like compounds (reaction 5).

1. $\text{LiPF}_{6(\text{sol})} \rightleftharpoons \text{LiF}_{(\text{sol})} + \text{PF}_{5(\text{sol})}$
2. $\text{LiPF}_{6(\text{sol})} + \text{ne}^- + \text{nLi}^+ \rightarrow \text{LiF} + \text{Li}_x\text{PF}_y$
3. $\text{LiPF}_{6(\text{sol})} + \text{H}_2\text{O} \rightarrow \text{LiF} + \text{POF}_3 + 2\text{HF}$
4. $\text{POF}_3 + \text{ne}^- + \text{nLi}^+ \rightarrow \text{LiF} + \text{Li}_x\text{POF}_y$
5. $\text{R-OH} + \text{PF}_5 \rightarrow \text{R-O-PF}_4 + \text{HF}$

Due to synthetic processes, sample II has a higher amount of coordination water, meaning that a higher amount of decomposition compounds should be expected, according to the proposed mechanism, as displayed in Figure 3b–d. As can be observed, the relative intensities regarding the degradation products are definitively higher in sample II in all investigated signals, thus confirming the difference in decomposition products due to hydration water. Table 4 summarizes all chemical shifts for the encountered species derived from the fitting procedure (in Table S2, literature references are summarized for comparison).

Table 4. Binding energies values for degradation products.

Assignment	Measured Binding Energy/eV		
	F 1s	Li 1s	P 2p
LiF	685.1	54.1	-
LiPF_6	688.8	58.4	137.8
Li_xPF_y	687.6	57.1	136.5
$\text{Li}_x\text{PO}_y\text{F}_z$	686.2	55.5	134.5–135
$-\text{PO}_x$	-	-	133.0
Teflon Area	684–693	-	-

Therefore, attributing the components at 58.4 eV (in Li 1s), 137.8 eV (in P 2p) and 688.8 (in F 1s) to LiPF_6 , it can be seen that its content is reduced from sample I to sample II, suggesting a higher degree of degradation. In particular, in sample II, the LiPF_6 contribution is barely detectable. Sample I tends to form $\text{Li}_x\text{PO}_y\text{F}_z$ products, while in the case of sample II a higher amount is recorded for Li_xPF_y . Finally, the quantity of obtained LiF is not dependent on the sample, since the relative quantity is similar in all of them (around 7–10%). Moreover, in P 2p a peak at 133 eV is also registered that has been assigned to $-\text{PO}_x$ -like species [40]. Sputter depth profiles were also attempted in order to reveal the structure close to the interface between electrolyte and electrode material. As shown in Figure S5, the main result is that the pure electrolyte forms a thin (maybe 1–2 nm) layer on the top of an interface layer containing the reaction products between the electrolyte and electrode. Due to the inherent obstacles of sputtering, no useful information about the oxidation state of the metals within this layer can be obtained.

Moreover, when the electrolyte is present, an increase in reduced species is registered as can be seen in Figure 4 from the ratio between Cu^+ and Cu^{2+} . This is indeed relevant in order to sustain the hypothesis of self-discharge of the material while storing the electrode for a certain period. However, care has to be taken when deriving such statements. First of all, it is always necessary to consider that the risk of radiation damage exists when highly energetic photons are employed for the excitation of the sample. In fact, the beam may lead to material degradation by altering their chemical nature [19]. In addition, the UHV conditions may cause additional damages if the material is not stable. In particular

hexacyanoferrates show sensibility and damaging while measuring and exposing to UHV ambience; Figure S6 shows the evolution of Cu centers upon increasing exposure time. To avoid artifacts when analyzing data, all the samples were evaluated after the same exposure time in order to be able to do proper comparisons. Assuring this, the data suggest that the electrolyte induces a reduction on the metal sites: this effect is due to the self-discharge of the electrode in contact with the electrolyte.

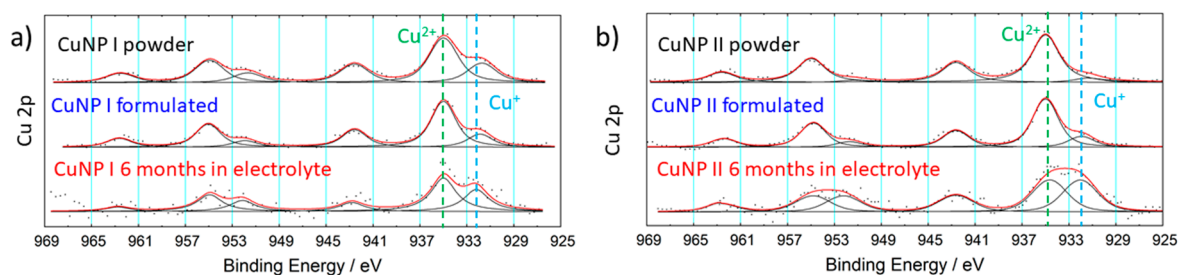


Figure 4. Effect of the presence of the electrolyte on the state of charge of metals. (a,b) Cu 2p signals of sample I and II.

It is also worth mentioning that both samples related to CuNP 6 months in electrolyte show very small Cu signals: this can be evidenced through the signal to noise ratio. Of course, this is obvious considering that growing films of degradation products attenuate the photoelectron intensity of the buried formulated electrode.

However, the same considerations cannot be done for Fe 2p signals. In fact, the F 1s plasmon loss peaks hinder proper evaluation.

X-ray absorption data at both Fe and Cu K-edges of samples I and II before and after contact with the electrolyte solution after six months are presented in Figure 5. Magnification plots of the pre-edge regions are shown as insets as well. Pristine and soaked (S) electrodes of sample I (Panels a and b) present similar features at both metal edges, although a slight difference in the Cu pre-edge (cf. inset of Panel b) can be identified in the small rising transition occurring at ~ 8981 eV. Concerning sample II, the $\text{Fe}^{\text{II}+\delta}/\text{Fe}^{\text{II}}$ reduction is evidenced by a shift of the edge position towards lower energies (cf. Panel c). Besides, by taking a closer look at the pre-edge region (cf. inset), the peak at 7114 eV shifts towards lower energy after contact with the electrolyte, and the weak peak at 7111 eV loses intensity. These findings suggest a different occupancy of the t_{2g} levels of the 3D orbitals, which is caused by the reduction of $\text{Fe}^{\text{II}+\delta}$ to Fe^{II} due to the self-discharge process triggered by the contact with the electrolyte solution. Panel d, similarly, compares the Cu K-edge features of sample II before and after soaking in the electrolyte. The evolution of the K-edge reflects the $\text{Cu}^{\text{II}}/\text{Cu}^{\text{I}}$ reduction—the peak centered at ~ 8981 eV and attributed to Cu^{I} species enhances in intensity, while the feature ascribed to Cu^{II} at ~ 8978 eV decreases [28,29,37,41–43]. The Cu reduction of the pristine electrode after being in contact with the electrolyte occurs also to a lesser extent for sample I, as described above. Overall, sample I shows a lower tendency to reduction after being in contact with the electrolyte than sample II.

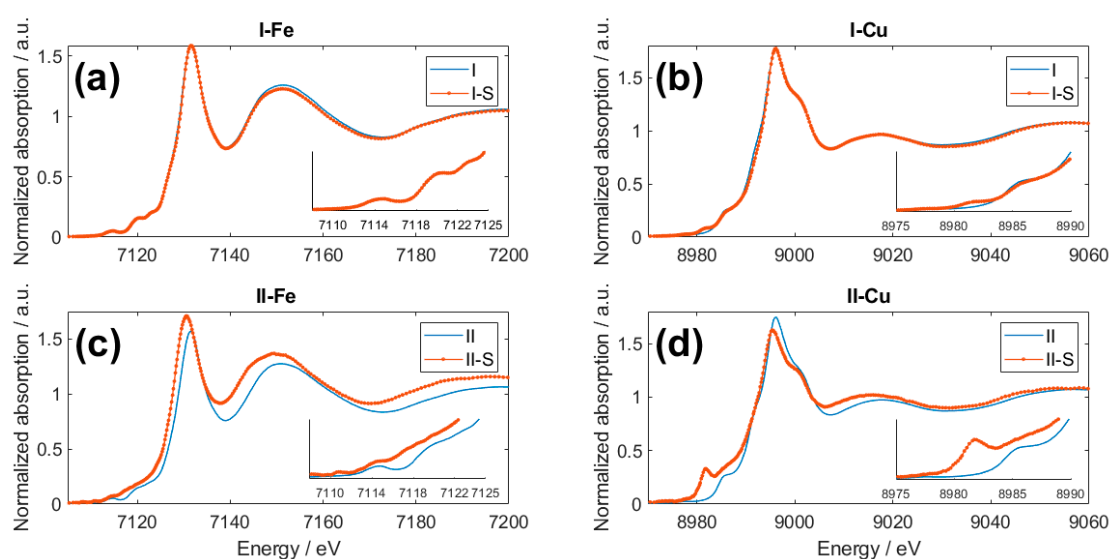


Figure 5. X-ray absorption spectroscopy spectra of samples I and II before and after contact with the electrolyte solution (S), taken at Fe and Cu K-edge after six months. (a) sample I at Fe K-edge (b) sample I at Cu K-edge (c) sample II at Fe K-edge (d) sample II at Cu K-edge.

4. Conclusions

This work highlights the chemistry at the surface of copper nitroprusside materials that are employed as cathodes in Li-ion batteries. The dynamics of the electrode was studied with an X-ray approach, employing both XPS and XAS techniques, which can gather complementary information (surface and bulk). XPS provided chemical analysis and speciation on the electrode surface after storage in a 1 M LiPF₆, EC/PC/3DMC electrolyte. In particular, insights into the chemical composition of surface film, which can be called cSEI, formed at ambient temperature, were provided. This film consists mainly of inorganic species and LiF, mostly coming from electrolyte decomposition products. The decomposition has been demonstrated to happen due to self-discharge processes only, with no need for cycling the cell. According to the proposed mechanisms, the sample with a higher amount of coordination water displays faster processes and a higher amount of degraded species. XAS data clearly support a chemical reduction at both metal sites, which takes place in the bulk of the material, whilst with XPS only Cu was evaluated, thus confirming the self-discharge process. The presence of a large amount of coordinated water in the electrode active material causes a greater tendency to reduction after being in contact with the electrolyte.

This, in turn, is clear evidence that a self-discharge process is occurring both on the surface and in the bulk of the two materials.

Supplementary Materials: The following are available online at <http://www.mdpi.com/1996-1073/13/15/4027/s1>, Figure S1: XPS fitted data for sample II. Figure S2: Pre-edge structure at the Fe K-edge. Figure S3: Pre-edge structure at the Cu K-edge. Figure S4: F 1s spectrum of sample I. Figure S5: XPS depth profile. Figure S6: XPS evolution of Cu 2p spectrum under UHV ambient. Table S1: Structural parameters from the EXAFS fitting. Table S2: Binding Energies of compounds.

Author Contributions: M.G. and R.D. performed the conceptualization and supervision of the research project. E.M. and P.H. performed XPS experiments. A.M., G.A. and M.G. performed XAS experiments. T.R. and R.D. revised the XPS part. E.M. and A.M. conducted data analysis. E.M., A.M. and M.G. wrote the paper. All the authors discussed the results and revised the text. All authors have read and agreed to the published version of the manuscript.

Funding: Measurements at ELETTRA were funded by the CERIC-ERIC, project number 20172042 (M. Giorgetti as PI). The Advanced Spectroscopy in Chemistry (ASC) European Joint Master Programme is acknowledged for enabling and financing the cooperation among the University of Leipzig and the University of Bologna. E.M. acknowledges the Erasmus+ scholarship for mobility.

Conflicts of Interest: The authors declare no conflict of interest.

References

1. Leonard, M.D.; Michaelides, E.E.; Michaelides, D.N. Energy storage needs for the substitution of fossil fuel power plants with renewables. *Renew. Energy* **2020**, *145*, 951–962. [[CrossRef](#)]
2. Goodenough, J.B.; Kim, Y. Challenges for rechargeable Li batteries. *Chem. Mater.* **2010**, *22*, 587–603. [[CrossRef](#)]
3. Elia, G.A.; Marquardt, K.; Hoepfner, K.; Fantini, S.; Lin, R.; Knipping, E.; Peters, W.; Drillet, J.F.; Passerini, S.; Hahn, R. An overview and future perspectives of aluminum batteries. *Adv. Mater.* **2016**, *28*, 7564–7579. [[CrossRef](#)] [[PubMed](#)]
4. Kiani, M.A.; Mousavi, M.F.; Rahmanifar, M.S. Synthesis of nano- and micro-particles of LiMn_2O_4 : Electrochemical investigation and assessment as a cathode in li battery. *Int. J. Electrochem. Sci.* **2011**, *6*, 2581–2595.
5. Tarascon, J.M.; Armand, M. Issues and challenges facing rechargeable lithium batteries. *Nature* **2001**, *414*, 359–367. [[CrossRef](#)]
6. Edström, K.; Gustafsson, T.; Thomas, J.O. The cathode-electrolyte interface in the Li-ion battery. *Electrochim. Acta* **2004**, *50*, 397–403. [[CrossRef](#)]
7. Duncan, H.; Abu-Lebdeh, Y.; Davidson, I.J. Study of the cathode–electrolyte interface of $\text{LiMn}_{1.5}\text{Ni}_{0.5}\text{O}_4$ synthesized by a Sol–Gel method for Li-Ion batteries. *J. Electrochem. Soc.* **2010**, *157*, A528. [[CrossRef](#)]
8. Malmgren, S.; Ciosek, K.; Lindblad, R.; Plogmaker, S.; Kühn, J.; Rensmo, H.; Edström, K.; Hahlin, M. Consequences of air exposure on the lithiated graphite SEI. *Electrochim. Acta* **2013**, *105*, 83–91. [[CrossRef](#)]
9. Andersson, A. Surface Phenomena in Li-Ion Batteries. Ph.D. Thesis, Uppsala University, Uppsala, Sweden, 2001.
10. Leanza, D.; Vaz, C.A.F.; Melinte, G.; Mu, X.; Novák, P.; El Kazzi, M. Revealing. The dual surface reactions on a HE-NCM Li-Ion battery cathode and their impact on the surface chemistry of the counter electrode. *ACS Appl. Mater. Interfaces* **2019**, *11*, 6054–6065. [[CrossRef](#)]
11. Lin, R.; Hu, E.; Liu, M.; Wang, Y.; Cheng, H.; Wu, J.; Zheng, J.C.; Wu, Q.; Bak, S.; Tong, X.; et al. Anomalous metal segregation in lithium-rich material provides design rules for stable cathode in lithium-ion battery. *Nat. Commun.* **2019**, *10*, 1–11. [[CrossRef](#)]
12. Malmgren, S.; Ciosek, K.; Hahlin, M.; Gustafsson, T.; Gorgoi, M.; Rensmo, H.; Edström, K. Comparing anode and cathode electrode/electrolyte interface composition and morphology using soft and hard X-ray photoelectron spectroscopy. *Electrochim. Acta* **2013**, *97*, 23–32. [[CrossRef](#)]
13. Yazami, R.; Reynier, Y.F. Mechanism of self-discharge in graphite-lithium anode. *Electrochim. Acta* **2002**, *47*, 1217–1223. [[CrossRef](#)]
14. Wang, L.; Menakath, A.; Han, F.; Wang, Y.; Zavalij, P.Y.; Gaskell, K.J.; Borodin, O.; Iuga, D.; Brown, S.P.; Wang, C.; et al. Identifying the components of the solid–electrolyte interphase in Li-ion batteries. *Nat. Chem.* **2019**, *11*, 789–796. [[CrossRef](#)] [[PubMed](#)]
15. Xu, K. Electrolytes and interphases in Li-ion batteries and beyond. *Chem. Rev.* **2014**, *114*, 11503–11618. [[CrossRef](#)]
16. Persson, K.; Sethuraman, V.A.; Hardwick, L.J.; Hinuma, Y.; Meng, Y.S.; Van Der Ven, A.; Srinivasan, V.; Kostecki, R.; Ceder, G. Lithium diffusion in graphitic carbon. *J. Phys. Chem. Lett.* **2010**, *1*, 1176–1180. [[CrossRef](#)]
17. Nie, M.; Chalasani, D.; Abraham, D.P.; Chen, Y.; Bose, A.; Lucht, B.L. Lithium ion battery graphite solid electrolyte interphase revealed by microscopy and spectroscopy. *J. Phys. Chem. C* **2013**, *117*, 1257–1267. [[CrossRef](#)]
18. Aurbach, D.; Markovsky, B.; Shechter, A.; Ein-Eli, Y.; Cohen, H. A comparative study of synthetic graphite and Li electrodes in electrolyte solutions based on ethylene carbonate-Dimethyl carbonate mixtures. *J. Electrochem. Soc.* **1996**, *143*, 3809–3820. [[CrossRef](#)]
19. Verma, P.; Maire, P.; Novak, P. A review of the features and analyses of the solid electrolyte interphase in Li-ion batteries. *Electrochim. Acta* **2010**, *55*, 6332–6341. [[CrossRef](#)]
20. Ventosa, E.; Madej, E.; Zampardi, G.; Mei, B.; Weide, P.; Antoni, H.; La Mantia, F.; Muhler, M.; Schuhmann, W. Solid electrolyte interphase (SEI) at TiO_2 electrodes in Li-Ion batteries: Defining *Apparent* and *Effective* SEI based on evidence from X-ray photoemission spectroscopy and scanning electrochemical microscopy. *ACS Appl. Mater. Interfaces* **2017**, *9*, 3123–3130. [[CrossRef](#)]

21. Hekmatfar, M.; Kazzazi, A.; Eshetu, G.G.; Hasa, I.; Passerini, S. Understanding the electrode/electrolyte interface layer on the Li-Rich nickel manganese cobalt layered oxide cathode by XPS. *ACS Appl. Mater. Interfaces* **2019**, *11*, 43166–43179. [[CrossRef](#)]
22. Erickson, E.M.; Li, W.; Dolocan, A.; Manthiram, A.; Erickson, E.M.; Li, W.; Dolocan, A.; Manthiram, A. Insights into the cathode-electrolyte interphases of high-energy-density cathodes in lithium-ion batteries. *ACS Appl. Mater. Interfaces* **2020**, *12*, 16451–16461. [[CrossRef](#)]
23. Kang, S.H.; Abraham, D.P.; Xiao, A.; Lucht, B.L. Investigating the solid electrolyte interphase using binder-free graphite electrodes. *J. Power Sources* **2008**, *175*, 526–532. [[CrossRef](#)]
24. Tsubouchi, S.; Domi, Y.; Doi, T.; Ochida, M.; Nakagawa, H.; Yamanaka, T.; Abe, T.; Ogumi, Z. Spectroscopic characterization of surface films formed on edge plane graphite in ethylene carbonate-based electrolytes containing film-forming additives. *J. Electrochem. Soc.* **2012**, *159*, A1786–A1790. [[CrossRef](#)]
25. Michan, A.L.; Leskes, M.; Grey, C.P. Voltage dependent solid electrolyte interphase formation in silicon electrodes: Monitoring the formation of organic decomposition products. *Chem. Mater.* **2016**, *28*, 385–398. [[CrossRef](#)]
26. Li, J.; Xing, L.; Zhang, L.; Yu, L.; Fa, W.; Xu, M.; Li, W. Insight into self-discharge of layered lithium-rich oxide cathode in carbonate-based electrolytes with and without additive. *J. Power Sources* **2016**, *324*, 17–25. [[CrossRef](#)]
27. Ware, M. Prussian blue: Artists' pigment and chemists' sponge. *J. Chem. Educ.* **2008**, *85*, 612. [[CrossRef](#)]
28. Mullaliu, A.; Aquilanti, G.; Conti, P.; Plaisier, J.R.; Fehse, M.; Stievano, L.; Giorgetti, M. Copper electroactivity in prussian blue-based cathode disclosed by operando XAS. *J. Phys. Chem. C* **2018**, *122*, 15868–15877. [[CrossRef](#)]
29. Mullaliu, A.; Sougrati, M.-T.; Louvain, N.; Aquilanti, G.; Doublet, M.-L.; Stievano, L.; Giorgetti, M. The electrochemical activity of the nitrosyl ligand in copper nitroprusside: A new possible redox mechanism for lithium battery electrode materials? *Electrochim. Acta* **2017**, *257*, 364–371. [[CrossRef](#)]
30. Hesse, R.; Chassé, T.; Szargan, R. Unifit 2002-universal analysis software for photoelectron spectra. *Anal. Bioanal. Chem.* **2003**, *375*, 856–863. [[CrossRef](#)]
31. Hesse, R.; Streubel, P.; Szargan, R. Product or sum: Comparative tests of Voigt, and product or sum of Gaussian and Lorentzian functions in the fitting of synthetic Voigt-based X-ray photoelectron spectra. *Surf. Interface Anal.* **2007**, *39*, 381–391. [[CrossRef](#)]
32. Yatsimirskii, K.B.; Nemoskalkenko, V.V.; Nazarenko, Y.P.; Aleshin, V.G.; Zhilinskaya, V.V.; Tomashevsky, N.A. Use of X-ray photoelectron and Mössbauer spectroscopies in the study of iron pentacyanide complexes. *J. Electron Spectros. Relat. Phenomena* **1977**, *10*, 239–245. [[CrossRef](#)]
33. Aquilanti, G.; Giorgetti, M.; Dominko, R.; Stievano, L.; Arçon, I.; Novello, N.; Olivi, L. Operando characterization of batteries using x-ray absorption spectroscopy: Advances at the beamline XAFS at synchrotron Elettra. *J. Phys. D Appl. Phys.* **2017**, *50*, 1–12. [[CrossRef](#)]
34. Cano, A.; Rodríguez-Hernández, J.; Shchukarev, A.; Reguera, E. Intercalation of pyrazine in layered copper nitroprusside: Synthesis, crystal structure and XPS study. *J. Solid State Chem.* **2019**, *273*, 1–10. [[CrossRef](#)]
35. Biesinger, M.C.; Lau, L.W.M.; Gerson, A.R.; Smart, R.S.C. Resolving surface chemical states in XPS analysis of first row transition metals, oxides and hydroxides: Sc, Ti, V, Cu and Zn. *Appl. Surf. Sci.* **2010**, *257*, 887–898. [[CrossRef](#)]
36. Gomez, A.; Rodriguez-Hernandez, J.; Reguera, E. Unique coordination in metal nitroprussides: The structure of Cu[Fe(CN)₅NO]·2H₂O and Cu[Fe(CN)₅NO]. *J. Chem. Crystallogr.* **2004**, *34*, 893–903. [[CrossRef](#)]
37. Mullaliu, A.; Aquilanti, G.; Stievano, L.; Conti, P.; Plaisier, J.R.; Cristol, S.; Giorgetti, M. Beyond the oxygen redox strategy in designing cathode material for batteries: Dynamics of a prussian blue-like cathode revealed by operando X-ray diffraction and X-ray absorption fine structure and by a theoretical approach. *J. Phys. Chem. C* **2019**, *123*, 8588–8598. [[CrossRef](#)]
38. Greczynski, G.; Hultman, L. Compromising science by ignorant instrument calibration-need to revisit half a century of published XPS data. *Angew. Chemie* **2020**, *132*, 5034–5038. [[CrossRef](#)]
39. Terborg, L.; Nowak, S.; Passerini, S.; Winter, M.; Karst, U.; Haddad, P.R.; Nesterenko, P.N. Ion chromatographic determination of hydrolysis products of hexafluorophosphate salts in aqueous solution. *Anal. Chim. Acta* **2012**, *714*, 121–126. [[CrossRef](#)]
40. Siow, K.S.; Britcher, L.; Kumar, S.; Griesser, H.J. XPS study of sulfur and phosphorus compounds with different oxidation states. *Sains Malays.* **2018**, *47*, 1913–1922.

41. Tisato, F.; Marzano, C.; Peruzzo, V.; Tegoni, M.; Giorgetti, M.; Damjanovic, M.; Trapananti, A.; Bagno, A.; Santini, C.; Pellei, M.; et al. Insights into the cytotoxic activity of the phosphane copper(I) complex $[\text{Cu}(\text{thp})_4][\text{PF}_6]$. *J. Inorg. Biochem.* **2016**, *165*, 80–91. [[CrossRef](#)]
42. Chaboy, J.; Muñoz-Páez, A.; Carrera, F.; Merklings, P.; Marcos, E.S. Ab initio x-ray absorption study of copper K -edge XANES spectra in Cu(II) compounds. *Phys. Rev. B* **2005**, *71*, 134208. [[CrossRef](#)]
43. Tomson, N.C.; Williams, K.D.; Dai, X.; Sproules, S.; Debeer, S.; Warren, T.H.; Wieghardt, K. Re-evaluating the Cu K pre-edge XAS transition in complexes with covalent metal-ligand interactions. *Chem. Sci.* **2015**, *6*, 2474–2487. [[CrossRef](#)]



© 2020 by the authors. Licensee MDPI, Basel, Switzerland. This article is an open access article distributed under the terms and conditions of the Creative Commons Attribution (CC BY) license (<http://creativecommons.org/licenses/by/4.0/>).